

Impact of jets on kilonova photometric and polarimetric emission from binary neutron star mergers

Manisha Shrestha¹,^{1,2}★ Mattia Bulla^{3,4,5,6}, Lorenzo Nativi⁶, Ivan Markin^{7,8}, Stephan Rosswog^{6,9} and Tim Dietrich^{7,10}

¹Steward Observatory, University of Arizona, 933 North Cherry Avenue, Tucson, AZ 85721-0065, USA

²Astrophysics Research Institute, Liverpool John Moores University, Liverpool Science Park IC2, 146 Brownlow Hill, L3 5RF Liverpool, UK

³Department of Physics and Earth Science, University of Ferrara, via Saragat 1, I-44122 Ferrara, Italy

⁴INFN, Sezione di Ferrara, via Saragat 1, I-44122 Ferrara, Italy

⁵INAF, Osservatorio Astronomico d'Abruzzo, via Mentore Maggini snc, I-64100 Teramo, Italy

⁶Department of Astronomy and Oskar Klein Centre, Stockholm University, AlbaNova, SE-10691 Stockholm, Sweden

⁷Institute for Physics and Astronomy, University of Potsdam, Haus 28, Karl-Liebknecht-Str 24/25, D-14476 Potsdam, Germany

⁸Leibniz Institute for Astrophysics Potsdam (AIP), An der Sternwarte 16, D-14482 Potsdam, Germany

⁹Hamburger Sternwarte, University of Hamburg, Gojenbergsweg 112, D-21029 Hamburg, Germany

¹⁰Max Planck Institute for Gravitational Physics (Albert Einstein Institute), Am Mühlenberg 1, D-14476 Potsdam, Germany

Accepted 2023 May 23. Received 2023 May 19; in original form 2023 March 24

ABSTRACT

A merger of binary neutron stars creates heavy unstable elements whose radioactive decay produces a thermal emission known as a kilonova. In this paper, we predict the photometric and polarimetric behaviour of this emission by performing 3D Monte Carlo radiative transfer simulations. In particular, we choose three hydrodynamical models for merger ejecta, two including jets with different luminosities and one without a jet structure, to help decipher the impact of jets on the light curve and polarimetric behaviour. In terms of photometry, we find distinct colour evolutions across the three models. Models without a jet show the highest variation in light curves for different viewing angles. In contrast to previous studies, we find models with a jet to produce fainter kilonovae when viewed from orientations close to the jet axis, compared to a model without a jet. In terms of polarimetry, we predict relatively low levels ($\lesssim 0.3$ – 0.4 per cent) at all orientations that, however, remain non-negligible until a few days after the merger and longer than previously found. Despite the low levels, we find that the presence of a jet enhances the degree of polarization at wavelengths ranging from 0.25 to $2.5\mu\text{m}$, an effect that is found to increase with the jet luminosity. Thus, future photometric and polarimetric campaigns should observe kilonovae in blue and red filters for a few days after the merger to help constrain the properties of the ejecta (e.g. composition) and jet.

Key words: gravitational waves – radiative transfer – techniques: photometric – techniques: polarimetric – (transients:) neutron star mergers.

1 INTRODUCTION

The merger of compact objects such as binary neutron star (NS) or black hole – NS systems can produce gravitational wave (GW) signals along with electromagnetic (EM) counterparts. This was confirmed by the 2017 August 17 detection of a short gamma-ray burst (GRB) 170817A (Goldstein et al. 2017; Savchenko et al. 2017) followed by the kilonova (KN) emission AT2017gfo (Coulter et al. 2017) in coincidence with the GW event GW170817 (Abbott et al. 2017) from the merger of a binary NS system. Due to a good localization of the event, many ground-based telescopes could follow up this watershed event throughout the entire EM spectrum (e.g. Alexander et al. 2017; Andreoni et al. 2017; Arcavi et al. 2017; Covino et al. 2017; Cowperthwaite et al. 2017; Drout et al. 2017; Evans et al. 2017; Haggard et al. 2017; Kasliwal et al. 2017; Margutti

et al. 2017; Pian et al. 2017; Smartt et al. 2017; Soares-Santos et al. 2017; Tanvir et al. 2017; Troja et al. 2017; Utsumi et al. 2017; Valenti et al. 2017). This event opened the new era of multimessenger astrophysics with GW sources.

KN emission is produced by the radioactive decay of the unstable heavy elements produced during the merger event and it was first predicted based on a simple, semi-analytical model by Li & Paczyński (1998). The optical emission from the KN can last for a few days, thus making it complementary to observations of short-lived GRB. These mergers are major sources of r-process elements (Lattimer & Schramm 1974; Symbalisty & Schramm 1982; Eichler et al. 1989; Freiburghaus, Rosswog & Thielemann 1999; Rosswog et al. 1999) and the neutron richness of the ejecta makes them in particular excellent candidates for the third r-process peak containing e.g. gold and platinum. Various groups identified the r-process elements in AT2017gfo (Watson et al. 2019; Domoto et al. 2021; Kasliwal et al. 2022), which points to either all or part of them being formed in binary NS mergers.

★ E-mail: ms1228@truman.edu

Even though these mergers are considered primary sources of heavy elements, there is only one confirmed KN observation in the form of AT2017gfo. There are a few possible candidates for KN such as KN associated with GRB 130603B (Tanvir et al. 2013) and GRB 211211A (Rastinejad et al. 2022; Troja et al. 2022). There are many open questions such as the density distribution of merger ejecta, distribution of lanthanide-rich material in the ejecta, and velocity of the ejecta. A combination of polarimetric and photometric studies will be crucial in improving our understanding of these open questions. Due to the lack of a wide array of observed KN, we need to rely on simulations to predict the properties of future KN observations as well as how to better equip various telescopes for efficient observations of these entities. There are various simulations that are designed for predicting spectra and light curves of KN emission (e.g. Kawaguchi, Shibata & Tanaka 2018; Wollaeger et al. 2018; Bulla 2019; Darbha & Kasen 2020; Korobkin et al. 2021; Collins et al. 2022) and few include polarization signal predictions (Matsumoto 2018; Bulla et al. 2019, 2021; Li & Shen 2019). We build on the work by Nativi et al. (2021) and Klion et al. (2021), where the impact of the jet on the ejected material and corresponding KN emission was investigated. In this paper, we add on to the models to make them more realistic by including a dynamical ejecta component and time-evolving opacities. Finally, we present both polarimetric and photometric results. We make use of the 3D Monte Carlo radiative transfer (MCRT) code POSSIS for the simulations (Bulla 2019, 2023).

The paper is organized as follows: in Section 2, we present the general method used for our simulation together with the simulation set-up of specific models. Then, we present results in Section 3, which is divided into photometric results (Section 3.1) and polarimetric results (Section 3.2). In Section 4, we discuss the implications of these results and how these results could be useful for future observation planning and analysis. Finally, we provide concluding remarks in Section 5.

2 METHODS

The simulations in this work are carried out using the latest (Bulla 2023) version of POSSIS (Bulla 2019), a 3D MCRT code that has been used in the past to predict polarization signatures of astrophysical transients as supernovae (Bulla, Sim & Kromer 2015; Inserra et al. 2016), KNe (Bulla et al. 2019, 2021), and tidal disruption events (Charalampopoulos et al. 2022; Leloudas et al. 2022). The code simulates the propagation of N_{ph} Monte Carlo (MC) photon packets throughout a medium expanding homologously and calculates flux and polarization spectra as a function of time t and observer viewing angle θ_{obs} . The energy of each MC packet is initialized by splitting into equal parts (Abbott & Lucy 1985; Lucy 1999) the total energy available from the radioactive decay of r-process nuclei, with heating rates taken from Rosswog & Korobkin (2022, see their equation 2) and thermalization efficiencies computed following Barnes et al. (2016) and Wollaeger et al. (2018). Each MC packet is assigned a normalized Stokes vector $\mathbf{s} = (1, q, u)$ that is initialized to $\mathbf{s}_0 = (1, 0, 0)$; i.e. packets are created with no polarization. The propagation of MC packets is controlled by the opacity of the expanding material. Time-dependent, state-of-the-art opacities from Tanaka et al. (2020) are adopted for both bound-bound line transitions, $\kappa_{\text{bb}}(\lambda, t, \rho, T, Y_e)$, and electron scattering, $\kappa_{\text{es}}(t, \rho, T, Y_e)$, as a function of local properties of the ejecta such as density ρ , temperature T , and electron fraction Y_e . MC packets are polarized by electron scattering and depolarized by bound-bound transitions, with their

Stokes vectors updated following Bulla et al. (2015). Spectra are extracted using ‘virtual’ packets as described in Bulla et al. (2015), with this technique reducing significantly the MC noise in the spectra compared to the angular binning of escaping packets more commonly adopted in the literature. We refer the reader to Bulla et al. (2015) and Bulla (2019, 2023) for more details about the code.

Polarization spectra are computed for three different models from Nativi et al. (2021). In these models, a neutrino-driven wind from Perego et al. (2014) has been evolved assuming that no jet (model Wind) or jets with opening angle $\theta_0 = 5^\circ$ and luminosity of $L_j = 10^{49} \text{ erg s}^{-1}$ (model Jet49) and $L_j = 10^{51} \text{ erg s}^{-1}$ (model Jet51) have been launched and propagated through the ejecta for 100 ms. In addition, all models include a spherical component at low velocities ($0.03\text{--}0.1c$, where c is the speed of light) accounting for ‘secular’ ejection mechanisms from the disc torus around the merger remnant (e.g. Beloborodov 2008; Just et al. 2015; Siegel & Metzger 2018; Fernández et al. 2019; Miller et al. 2019). This component is relatively massive ($M_{\text{sec}} = 0.072 M_\odot$) and in this work assumed to have a fixed $Y_e = 0.35$, although the detailed composition of the secular ejecta is still a matter of debate (e.g. Siegel & Metzger 2018; Miller et al. 2019). The main focus of this work is the polarimetric behaviour of KN emission; hence, we do not investigate the lanthanide-rich composition explored in Nativi et al. (2021) as it would lead to a null polarization signal due to electron scattering being subdominant (see discussion in Bulla et al. 2019). Compared to Nativi et al. (2021), here we model an additional component to account for material ejected dynamically. Specifically, we assume a dynamical ejecta component with a mass $M_{\text{dyn}} = 0.005 M_\odot$, a lanthanide-rich composition ($Y_e = 0.15$), and a distribution extending from $0.1c$ to $0.3c$ and in a conical region around the merger plane with half-opening angle $\phi = 30^\circ$.

Density, Y_e , temperature, and opacity maps at 1 d after the merger are shown in Fig. 1 for the three different models. We outline regions in Jet49 and Jet51 important for interpreting the polarization signals – the regions of the wind material propelled by the jet at $\theta \sim 25^\circ$ from the polar axis, with high Y_e and dominated by electron scattering (light grey contours in the right-hand panels of Fig. 1). These regions are more extended in the Jet51 compared to the Jet49 model. Hereafter, we refer to these regions as electron-scattering plumes.

Radiative transfer simulations presented in this work are carried out for $N_{\text{ph}} = 5 \times 10^8$ MC photons and for a grid resolution of 128^3 for all three models. Flux and polarization spectra are extracted for 100 time bins logarithmically spaced from 0.1 and 30 d after the merger, 1000 wavelength bins logarithmically spaced from 0.05 to $10 \mu\text{m}$ and 11 viewing angles equally spaced in cosine from $\cos \theta_{\text{obs}} = 1$ (face-on, along the jet axis) to $\cos \theta_{\text{obs}} = 0$ (edge-on, in the merger plane). Since the models are axially symmetric around the jet axis, the polarization signal is carried by Stokes q while Stokes u is consistent with zero, and its signals are used as a proxy for MC noise.

The modelling performed here is an improvement over previous studies in various respects. First, we take into account time-dependent effects that were not considered in polarization studies of Bulla et al. (2019, 2021), in which ejecta properties (including opacities) were frozen at selected epochs. Secondly, we model all the main components expected in binary NSs mergers – jet, wind, dynamical, and secular ejecta – instead of restricting to a broad two-component model as done e.g. in Bulla et al. (2019). Finally, we adopt state-of-the-art opacities as a function of local properties of the ejecta (see above) in place of uniform values in each component as done in both

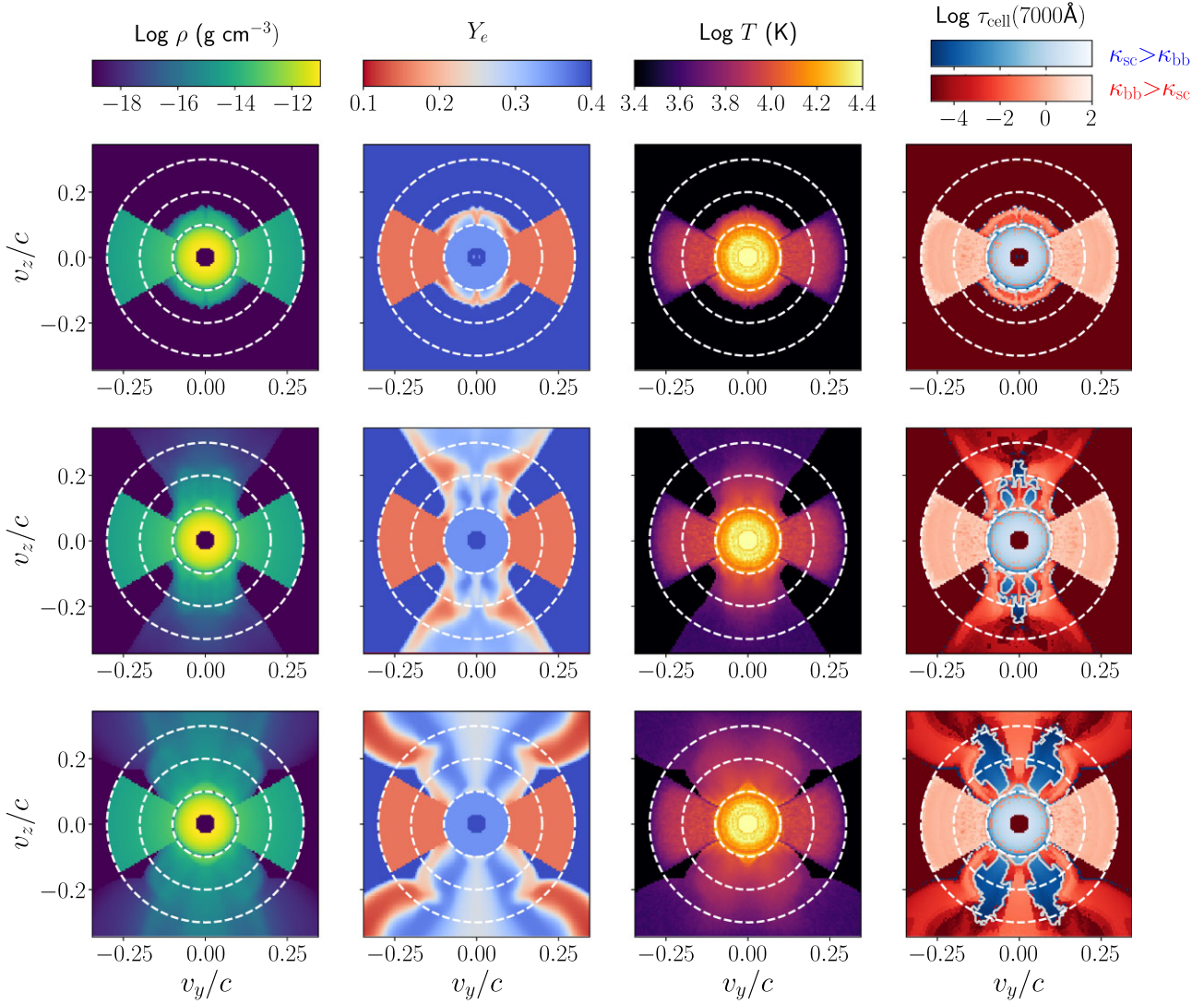


Figure 1. Model properties at 1 d after merger for Wind (top), Jet49 (middle), and Jet51 (bottom). From left to right, maps in the velocity v_y - v_z plane are shown for the density ρ , the electron fraction Y_e , the temperature T , and the optical depth at 7000 Å within each cell $\tau_{\text{cell}} = (\kappa_{\text{es}} + \kappa_{\text{bb}}) \rho dr$, where κ_{es} and κ_{bb} are the Thomson scattering and bound-bound opacities, respectively, and dr is the cell width. The optical depths are shown in red (blue) colours for cells where bound-bound opacity is larger (smaller) than electron-scattering opacity. Light grey contours in the right-hand panels highlight the electron-scattering plumes where electron-scattering opacity is dominant over bound-bound opacity. Dashed white circles mark velocities of 0.1, 0.2, and 0.3c. All the models have a 128^3 grid resolution.

Bulla et al. (2019, 2021) or approximate analytical functions as done in Nativi et al. (2021).

3 RESULTS

In this section, we present the results from the three models described in Section 2. First, we present the photometric results in Section 3.1 and then provide the polarimetric results in the form of spectropolarimetry and polarimetric curve in Sections 3.2.1 and 3.2.2, respectively.

3.1 Photometry

From the spectral time series obtained with POSSIS, we can construct light curves for different filters and different viewing angles. In Fig. 2, we present the results for three models: Wind, Jet49, and Jet51.

Different panels in Fig. 2 refer to the different filters u , g , r , i , z , J , H , and K . Each panel has light curves for different inclination angles going from 0° to 90° represented by dark blue to yellow colours, respectively. We have included observed data of AT2017gfo as open circles in our light curve to present comparative values to the readers. However, we are not doing a rigorous comparison between our model and AT2017gfo data, and there is no reason to expect that the employed models have to describe the AT2017gfo observation.

The time evolutions of the light curves of Jet49 and Jet51 show a similar trend to the Wind model. However, the variation in apparent magnitude with respect to the inclination angle is smaller in the models with a jet compared to models without a jet, an effect that was also seen by Nativi et al. (2021). This behaviour can be understood based on the opacity distribution of these models as shown in Fig. 1. As shown in the opacity maps, the presence of a jet distributes some optically thick material from the wind component

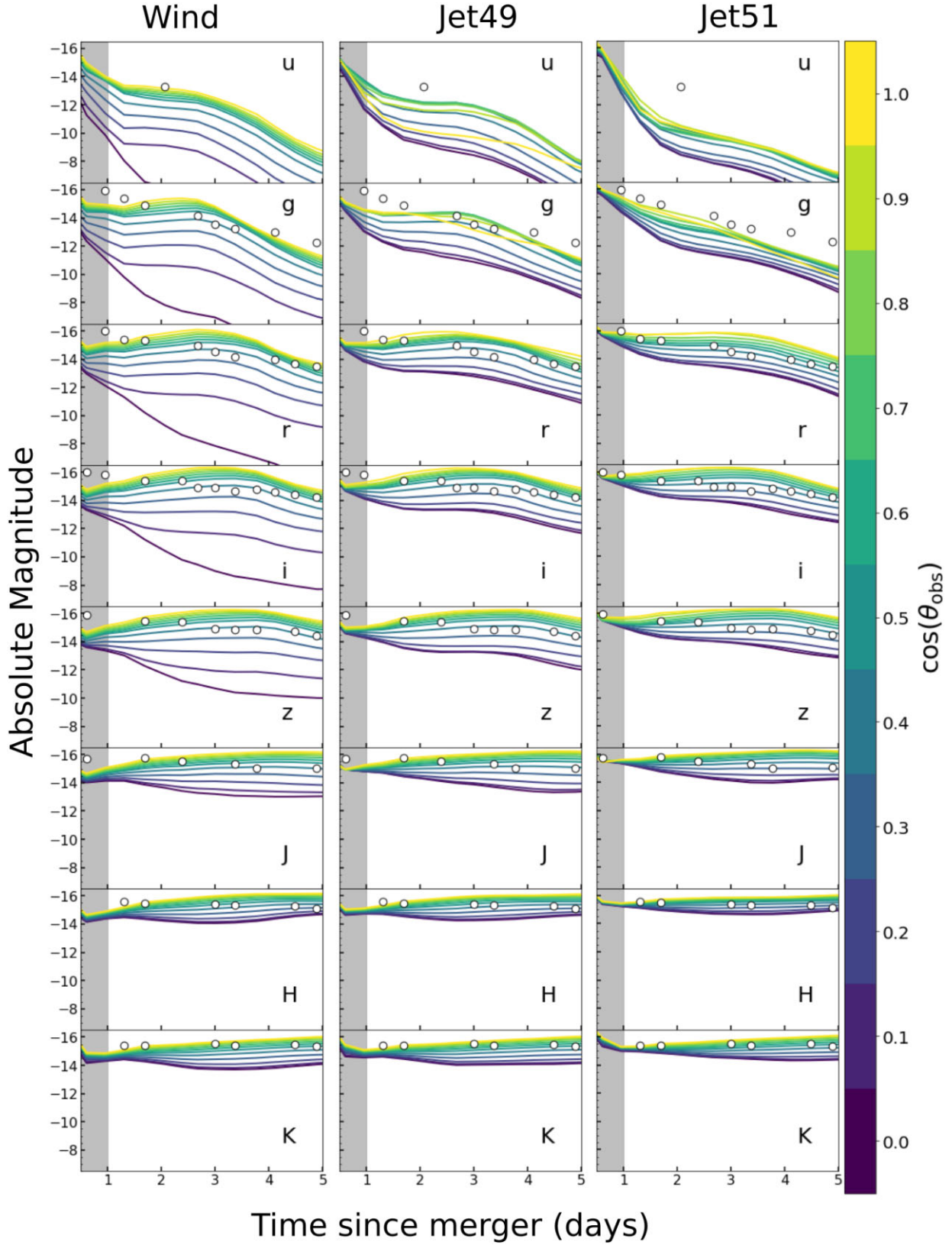


Figure 2. Broad-band *ugrizJHK* light curves of three models Wind (left), Jet49 (middle), and Jet51 (right). Different coloured lines represent the light curve at various inclination angles. The open circle is the observational data of AT2017gfo which has been corrected for the Milky Way extinction using Schlafly & Finkbeiner (2011). The shaded grey region represents the time period up to 1.0 d after the merger where opacity calculations are not highly reliable (Tanaka et al. 2020).

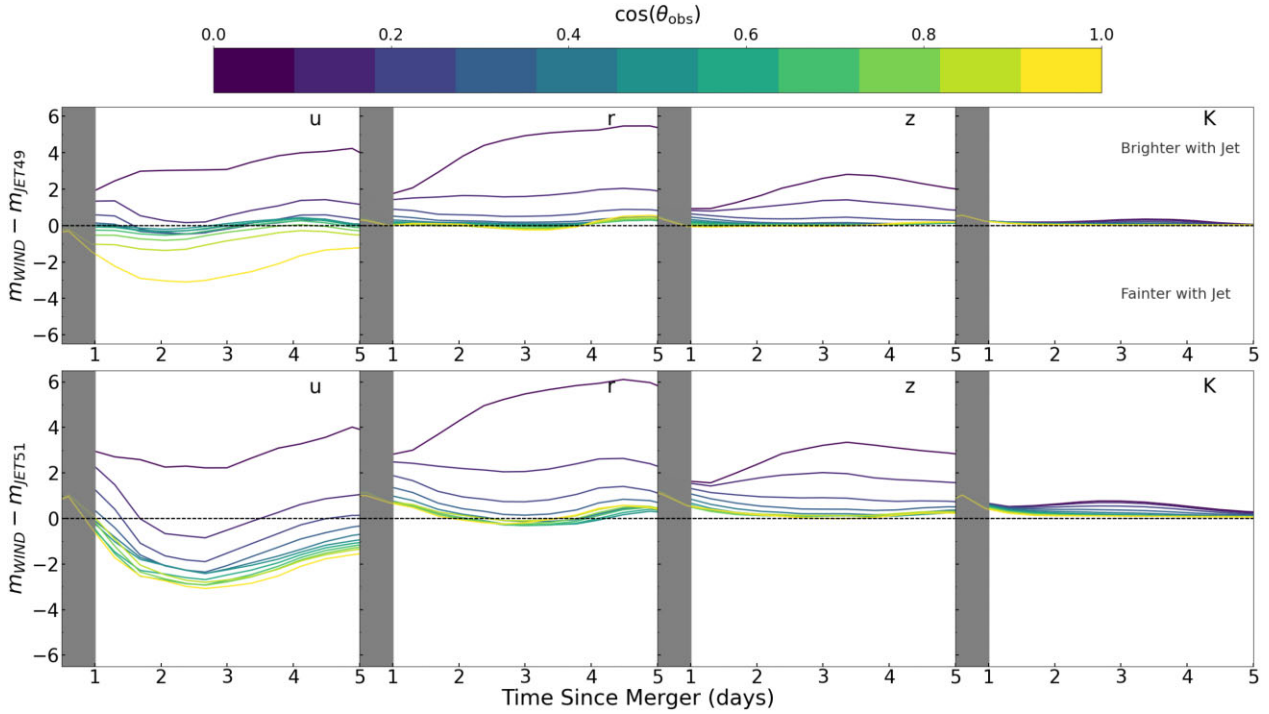


Figure 3. Difference in magnitude for different filters for the jet models compared to wind model. The top plot is for the difference in Wind and Jet49 magnitude and the bottom is for the difference in Wind and Jet51 magnitude. The eight different panels are for different filters *urzk*, respectively. As in Fig. 2, different coloured lines in each panel represent different inclination angles ranging from 0° to 90° from dark blue to yellow, respectively. We have labelled the regions below and above the zero as the case where Jet models are fainter and brighter than the Wind model which is true for both panels.

to higher velocities ($\gtrsim 0.1c$). Therefore, some of the photons emitted towards the polar regions can get scattered/reprocessed to other angles. In addition, regions of the wind which in the Wind model were obscured by the dynamical ejecta when viewed from equatorial viewing angles are now exposed to these orientations in the Jet49 and Jet51 models. Compared to the wind case, the KN with the jet cases is, therefore, fainter at polar angles and brighter at equatorial/intermediate angles, effectively reducing the viewing angle dependence. This effect can also be seen in the magnitude differences presented in Fig. 3. These predictions are in contrast to those by Nativi et al. (2021) and Klion et al. (2021) and will be further discussed in Section 4.

The evolution of light curves in different filters for all the models is similar in nature. We see that for shorter wavelengths *u* and *g*, the brightness decreases with time for all the inclination angles. However, the sharpness of the decrease in brightness is dependent on the type of model. For the case of Wind, the decrease in brightness is gradual, for Jet49 the decrease is sharper and the decrease is the sharpest for Jet51. This can be explained by the variation in scattering opacity along the jet axis based on wavelengths with time. The opacity is higher in shorter wavelengths (*u* and *g*) and it increases with time. Thus, more photons with shorter wavelengths are scattered. Therefore, only a small portion of photons in this wavelength regime can escape for the models with jet, which produces the rapid decline in brightness in *u* and *g* filters. In *r*, *i*, *z*, *J*, *H*, *K* filters, there is an initial decline in brightness followed by an increase and then a plateau for viewing angles closer to the equatorial plane. For polar viewing angles, the brightness increases and then plateaus. Both equatorial and polar behaviour can be explained in terms of optical depth evolution. As time evolves, the optical depth decreases, thus the multiple interacting photons from earlier times are

able to escape from the simulation grid. As photons are reprocessed by lines, they are re-emitted at longer wavelengths. Hence, the KN signal is higher at these longer wavelengths.

3.2 Polarimetry

One of the main aims of the paper is to study the impact of a jet on polarization signal from KNe emission. From the simulations described in Section 2, we get polarimetric information in the form of Stokes vectors *q* and *u*. Since the models are symmetric around the jet axis, Stokes *u* is expected to be zero, and Stokes *q* quantifies the polarization signal. We can create polarization spectra as shown in Fig. 4 and from that, we can create a broad-band polarimetric curve as shown in Fig. 5. In this section, we present the polarimetric results for the three different models Wind, Jet49, and Jet51.

3.2.1 Polarization Spectra

In Fig. 4, we present the variation for Stokes *q* with respect to wavelengths for the three different models Wind, Jet49, and Jet51 for four selected time epochs of 1.3, 2.4, 3.8, and 4.2 d after the merger and four different inclination angles of $\theta_{\text{obs}} = 26^\circ$, 66° , 73° , and 90° . We see that polarization is highly dependent on the inclination angle and the evolution with time for the three models is different from each other.

For the case of Wind, we mostly detect very low levels of Stokes *q* for all the filters and viewing angles and we detect some higher scatter at day 1.3 after the merger. Since the error bar is larger, we can attribute this mostly to MC noise. The highest level of polarization is seen for the intermediate angle of $\theta_{\text{obs}} = 73^\circ$, with a low Stokes *q* ~ -0.28 per cent at 2.4 d after the merger. The low level of

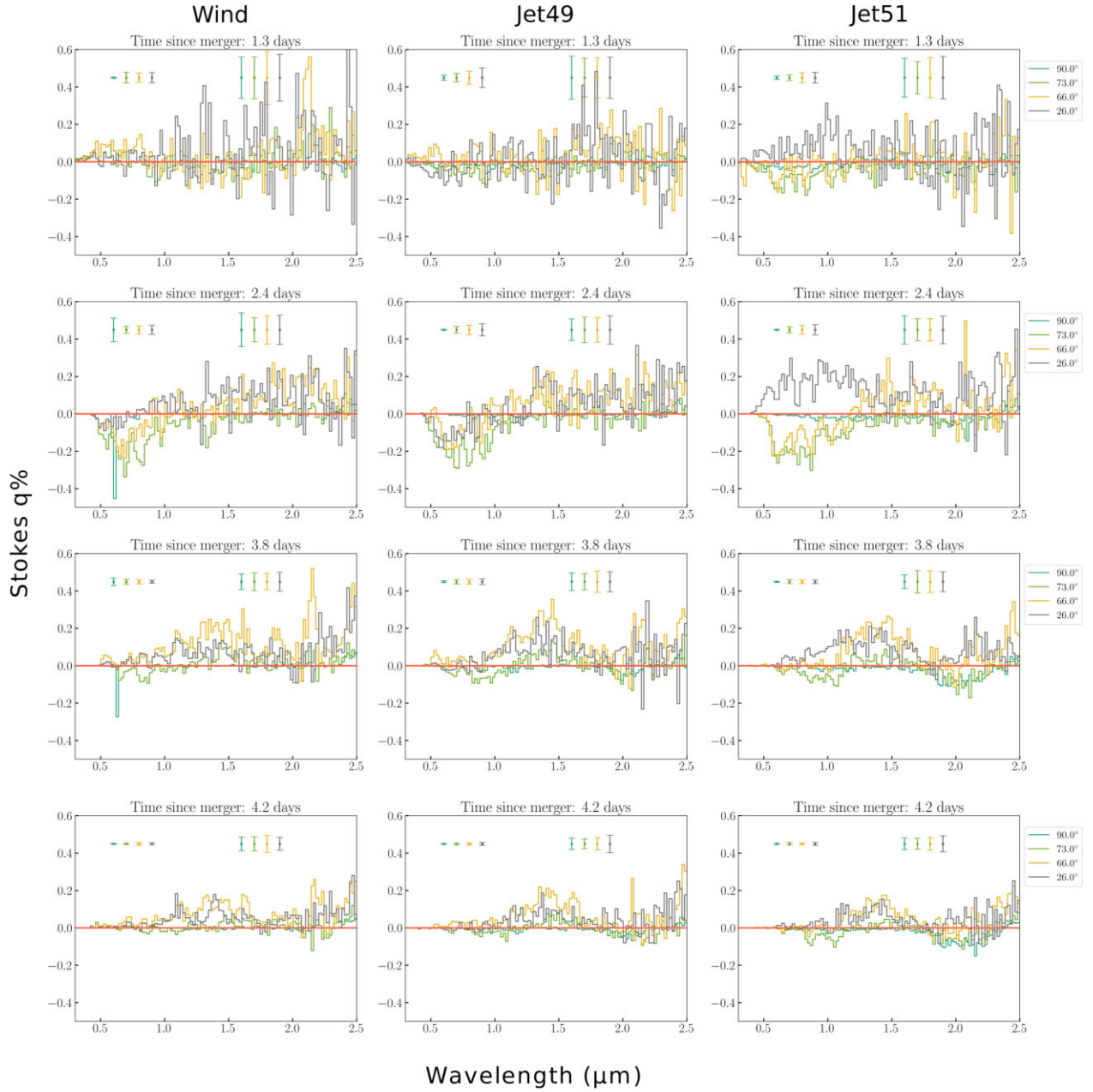


Figure 4. Spectropolarimetric curves for the three different models from left to right. Different panels from top to bottom is for different time since the merger, and different colour curves in each panel represent different viewing angles. The scatter in Stokes u is assumed to be the error in Stokes q . For each viewing angle, we present one error value for wavelengths shorter than $1.5 \mu\text{m}$ in the top-left corner of each panel and another error bar for longer wavelengths in the top-right corner.

polarization can be understood from the opacity map shown in Fig. 1. The region with dominant electron-scattering opacity, i.e. blue region is associated with the secular component, is mostly concentrated around the core, and is spherically symmetric. The photons that are scattered from this portion have to go through the higher density regions with the possibility of absorption or multiple scattered. This can cause the polarization value to be lower. The small polarization signal in q is comparable to the u signal shown as error bars in the plot. This shows that the signal in Stokes q is compatible with MC noise.

For the Jet49 model, the highest polarization values are seen for $\theta_{\text{obs}} = 26^\circ$ and 66° at wavelengths shorter than $1.0 \mu\text{m}$ in earlier time

periods. At 2.4 d after the merger, a polarization signal of negative 0.3 per cent is seen which decreases on 3.8 d after the merger with a polarization signal closer to negative 0.25 per cent. On days 3.8 and 4.2 after the merger, we see some positive polarization signal at wavelengths longer than $1.25 \mu\text{m}$ as shown in Fig. 4. This could be attributed to photons that emerge from lanthanide-rich dynamical ejecta at late times and infrared (IR) wavelengths and are scattered by electron-scattering plumes before reaching the observer. Initially, the density of dynamical ejecta in the equatorial plane is extremely high, thus the photons scattered in dynamical ejecta cannot escape the simulation grid in earlier days like 1.3 and 2.4 d after the merger. However, the electron-scattering opacity is higher in regions close to

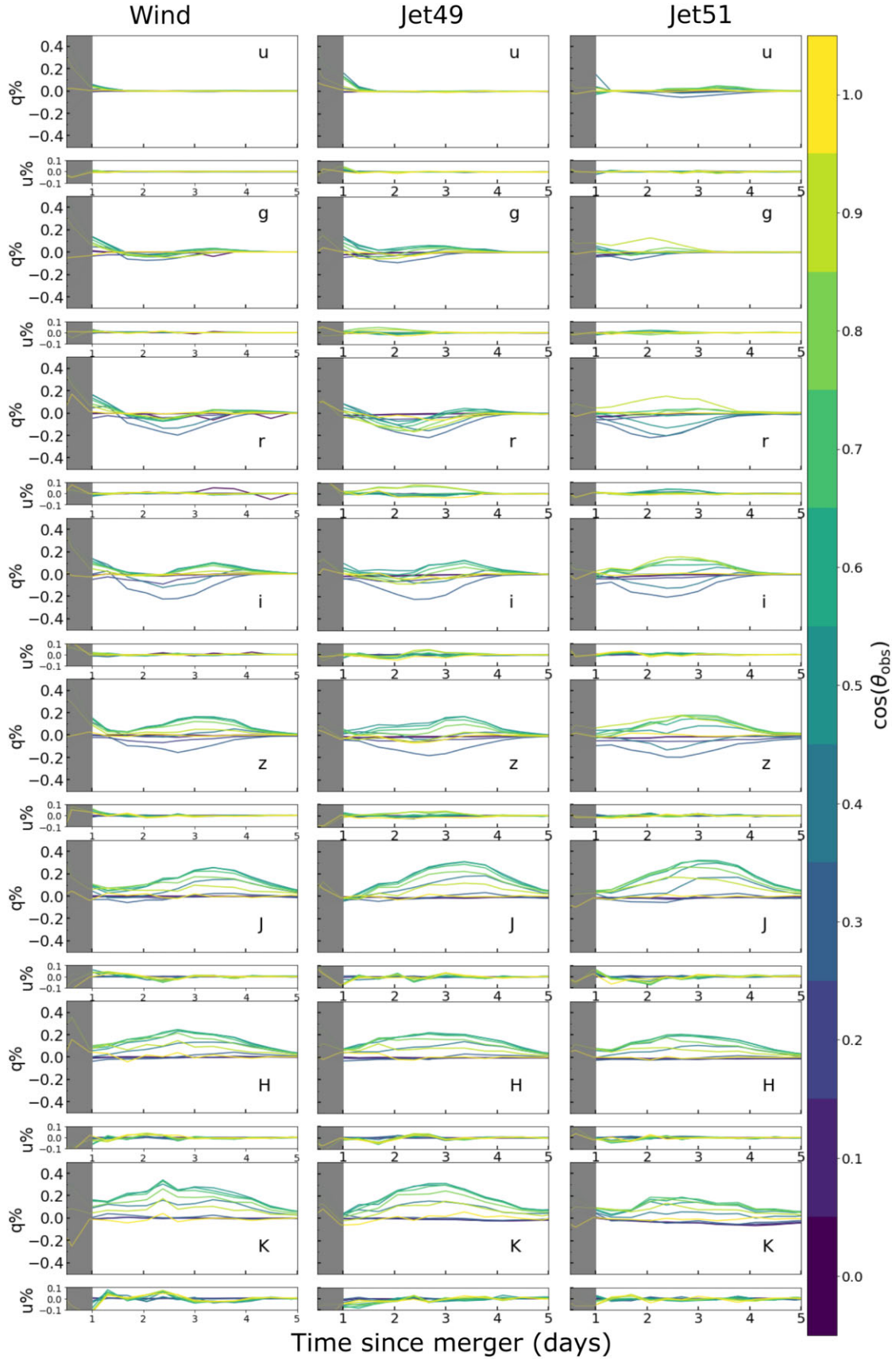


Figure 5. Plot of % q and % u with respect to time for $ugriz$ broad-band filters. Three columns of plots are for three different models. The colour of different curves represents the different inclination angles. The shaded grey region represents the time period of 0.5–1.0 d after the merger where opacity calculations are not highly reliable.

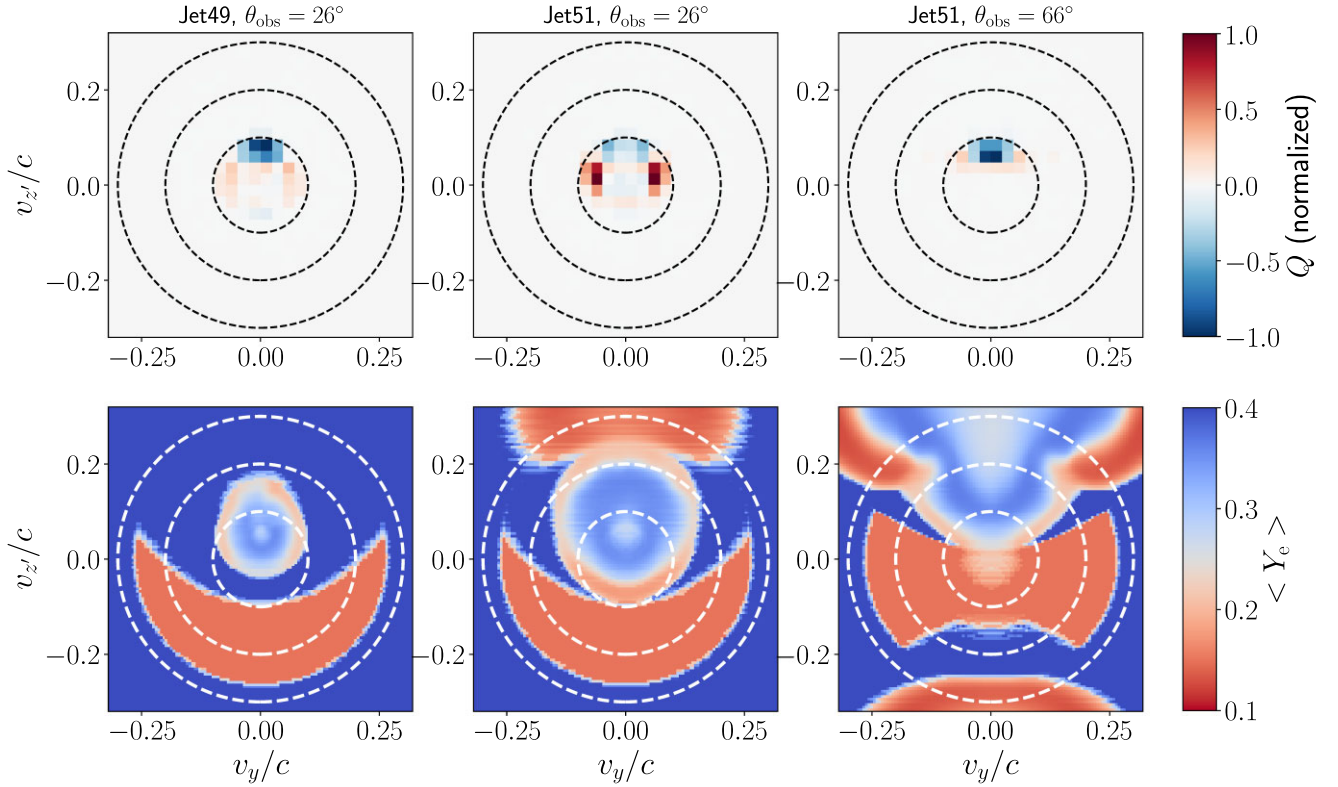


Figure 6. Q maps (top) versus Y_e maps (bottom) for three cases from Fig. 4 showing non-zero polarization levels around 2 d after the merger and at $\sim 7000 \text{ \AA}$: the Jet49 model viewed from 26° with $q < 0$ (left), the Jet51 model viewed from 26° with $q > 0$ (middle), and the Jet51 viewed from 66° with $q < 0$ (right). All maps are calculated by rotating the xyz Cartesian grid about the y -axis and so that x' corresponds to the line of sight to the given observer, i.e. $x' = x \cos(\pi/2 - \theta_{\text{obs}}) + z \sin(\pi/2 - \theta_{\text{obs}})$, $y' = y$, and $z' = -x \sin(\pi/2 - \theta_{\text{obs}}) + z \cos(\pi/2 - \theta_{\text{obs}})$. The Q maps are computed by integrating all the contributions along the line of sight and are normalized to the maximum value across the three cases. The Y_e maps are computed by averaging the Y_e values from 0.075 to 0.15 c along the line of sight and on the approaching side of the ejecta. Dashed white circles mark velocities of 0.1, 0.2, and 0.3 c as in Fig. 1.

the jet axis as shown by the blue regions or the electron-scattering plumes in Fig. 1. This can scatter photons and produce a polarized signal. Since the photons are getting scattered from polar regions, the scattered photons have preferentially negative Stokes q which can be seen in Fig. 6. There are a few photons that can escape the grid in earlier times with less scattering, hence this negative Stokes q is seen for shorter wavelength. As time increases, the densities in the dynamical ejecta decrease and the photons that are scattered from the electron-scattering plume region can escape with a positive sign in their Stokes q .

The Jet51 model shows higher levels of polarization for all the wavelengths on 2.4 d after the merger compared to Wind and Jet49 case. This directly relates to a larger region of electron-scattering plumes. At 1.3 d after the merger, there is no clear polarization signal. However, we predict negative Stokes q for $\theta_{\text{obs}} = 66^\circ$ and 73° and for wavelength less than $0.85 \mu\text{m}$ which can also be seen in Fig. 6 for the epoch of 2.4 d after the merger. For $\theta_{\text{obs}} = 26^\circ$, there is some positive Stokes q signal. For the other epochs, the polarization signal for this model is similar to cases of Wind and Jet49.

3.2.2 Polarization curves

The results from Section 3.2.1 can be converted to polarization curves for different broad-band filters ($ugriz$) as shown in Fig. 5. Due to the wider availability of imaging polarimeters compared to spectropolarimeters and imaging polarimetry requiring fewer photons for better polarization accuracy, polarization curve predictions can

be crucial from an observational standpoint. Hence, in this section, we present the prediction of polarization evolution with time for various optical and near-IR filters. Different colours in each panel are for different inclination angles.

The Wind model's polarization curve in Fig. 5 (left-hand panels) shows mostly a low level of polarization signal. We see a slight increase in polarization at later times for longer wavelengths like *rizJHK* filters and the noise level is low as well indicating it to be an actual polarization signal. For viewing angles closer to the edge-on, we detect some negative Stokes q which is more prominent in *riz* filters up to 3 d after the merger with the peak at 2.5 d after the merger with values between 0.2–0.25 per cent. After 2.5 d, we detect positive Stokes q ($\lesssim 0.3$ per cent) for viewing angle towards the polar regions for *JHK* filters. Higher polarization in longer wavelengths at later times can be attributed to multiple interacting photons escaping at later times from higher opacity dynamical ejecta regions. The polarization signal about the inclination angle of 0° is very close to zero due to the symmetry of the geometry. Hence, the signal we are getting of a few per cent is real and not MC noise.

The polarization curves of Jet49 are presented in Fig. 5 (middle panels). The polarization curve for *ug* filters shows an insignificant polarization degree. We see a low level of polarization in *r*, *i*, *z*, *J*, *H*, and *K* filters ($q \lesssim 0.3$ per cent). For *r*, *i*, and *z* filters, we see negative Stokes q for days 1 to 3 after the merger. Unlike Wind model, here the negative Stokes q is also seen for viewing angles closer to polar viewing angle. We note that for *riz* filters, we see a significant level of noise during this period, thus we contribute this signal to MC noise.

For *JHK* filters, the positive Stokes q is not accompanied by high noise, thus we believe these signals to be real.

Fig. 5 (right-hand panels) shows the results for simulation of the *Jet51* model. In general, we see a slightly higher level of polarization signal for this model compared to the previous two models. For u and g filters, we do not see any clear polarization detection. However, for *rizJHK* filters, we see mostly positive Stokes q lower than 0.35 per cent for the viewing angles closer to the polar region. Whereas for more edge-on viewing angles, we detect some negative Stokes q . The polarization peak is between 2 and 3 d since the merger for the *riz* filter. For longer wavelengths *JHK*, there is no clear peak and we see a constant polarization signal of 0.2 per cent from day 1 to day 5 after the merger.

4 DISCUSSIONS

Overall, our knowledge of the properties of KN emission is limited. To improve our understanding, we performed 3D MCRT simulations to predict the photometric and polarimetric behaviour for three different models, namely *Wind*, *Jet49*, and *Jet51*. From these simulations, we presented light curves for 11 different inclination angles from 0° to 90° for u , g , r , i , z , J , H , and K filters. In addition, we also presented spectropolarimetric results along with polarization curves. We have made improvements in previous models presented in Bulla et al. (2019, 2021) by including all the main components expected in binary NS mergers. In addition, the models are updated to include the time evolution of ejecta properties such as opacity, density, temperature, and they include time- and electron fraction-dependent nuclear heating rates (Rosswog & Korobkin 2022).

Our models build on the set-up from Nativi et al. (2021) for the case of the lanthanide-poor disc with the addition of an extra component of lanthanide-rich dynamical ejecta and improved opacities. Our light-curve behaviour is different from what was reported in Nativi et al. (2021) (fig. 4 in their paper). The light curves from our simulations have higher apparent magnitude compared to the previous results in Nativi et al. (2021). The values presented in this paper are closer to the apparent magnitude observed for GW 170817 KN AT2017gfo (Andreoni et al. 2017; Arcavi et al. 2017; Chornock et al. 2017; Cowperthwaite et al. 2017; Drout et al. 2017; Evans et al. 2017; Kasliwal et al. 2017; Pian et al. 2017; Smartt et al. 2017; Tanvir et al. 2017; Troja et al. 2017; Utsumi et al. 2017; Valenti et al. 2017). In both cases, the variation with inclination angles is greatest for the *Wind* model. However, the overall variation with viewing angle is much higher in our results. This behaviour can be attributed to the variation in ejecta density distribution. Due to the presence of dynamical ejecta with higher density, polar viewing angles are always brighter than viewing angles closer to the equator.

In contrast to previous studies (Klion et al. 2021; Nativi et al. 2021), we do not see the presence of a jet making the light curve brighter near the polar viewing angle. On the contrary, we find that the presence of a jet leads to a decrease in brightness for orientations close to the jet axis and an increase in brightness for more equatorial viewing angles. As shown in Fig. 7 for the *Jet51* case, this effect is due to the difference in opacity set-up for models in this paper. For the opacities, Nativi et al. (2021) used simple analytical functions and a bimodal uniform distribution (lanthanide-poor + lanthanide-rich depending on whether Y_e was larger or smaller than 0.25, respectively, Bulla 2019), leading to ejecta that were optically thin in the regions where material from the wind are spread out by the jet ($\gtrsim 0.15c$, orange squares). In contrast, the state-of-the-art opacities from Tanaka et al. (2020) used in this work depend on local properties

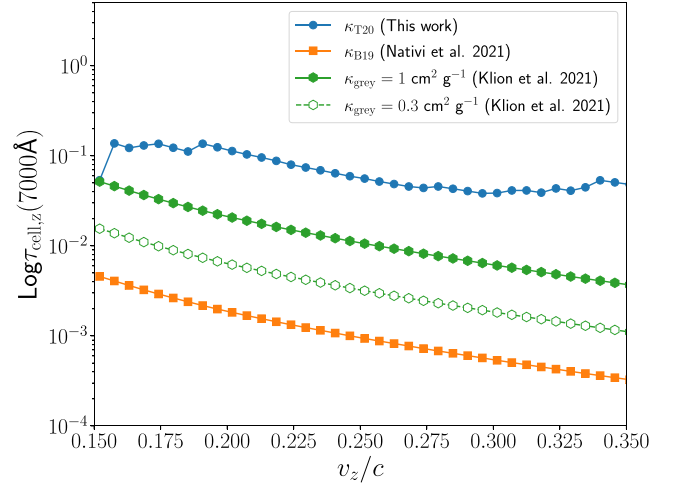


Figure 7. Optical depth within a cell as a function of velocity along the z (jet) axis. Curves are shown for the *Jet51* model and for different assumptions for the opacities κ : state-of-the-art opacities from Tanaka et al. (2020) adopted in this work (κ_{T20} , blue circles), analytical and uniform opacities from Bulla (2019) adopted in Nativi et al. (2021) (κ_{B19} , orange squares), grey opacities with $\kappa_{\text{grey}} = 1 \text{ cm}^2 \text{ g}^{-1}$ adopted in Klion et al. (2021) (filled green hexagons), and grey opacities with $\kappa_{\text{grey}} = 0.3 \text{ cm}^2 \text{ g}^{-1}$ (open green hexagons) found to reproduce well-detailed iron-group-like opacities used in Klion et al. (2021, see their fig. 9). Optical depths are calculated within each cell at 1 d after the merger. For the two sets of non-grey opacities, optical depths are calculated at 7000 \AA as $\tau_{\text{cell}} = (\kappa_{\text{es}} + \kappa_{\text{bb}}) \rho dr$, where κ_{es} and κ_{bb} are the Thomson scattering and bound-bound opacities, respectively, and dr is the cell width.

of the ejecta (ρ , T , and Y_e) and lead to moderately optically thick regions for a wide range of velocity above $\gtrsim 0.15c$ (cyan squares). The integrated optical depth from $0.15c$ to the grid boundary at 1 d after the merger is equal to ~ 2.68 in our work while ~ 0.05 when using the opacities in Nativi et al. (2021). Hence, in our work, photons that are emitted towards polar viewing angles can get scattered by material redistributed by the jet close to the jet axis and re-emitted with longer wavelengths towards the equatorial viewing angles, decreasing (increasing) the KN brightness for face-on (intermediate/edge-on) view of the system. Although we do not have information about optical depths in the models by Klion et al. (2021), we note that adopting in our models their grey opacities $\kappa_{\text{grey}} = 1$ and $\kappa_{\text{grey}} = 0.3 \text{ cm}^2 \text{ g}^{-1}$ (found to reproduce well their simulation with iron-group-like opacities) would lead to optically thin ejecta along the jet axis as in Nativi et al. (2021) (filled and open green hexagons, respectively). Although the opacities that we used in this work (Tanaka et al. 2020) are more reliable than those employed in Nativi et al. (2021) and Klion et al. (2021), it is worth stressing that large uncertainties in r-process opacities remain, and it is difficult to quantify by how much our light-curve results may be impacted by them.

This work also examined the impact of jets and dynamical ejecta on polarization signals. We present spectropolarimetry and polarization curves for the three different models. One of the major differences compared to previous results from Bulla et al. (2019, 2021) is that the polarization signal is present even at relatively late times like 2–3 d after the merger. This can be attributed to the difference in the opacity implementation in the simulations presented in this paper compared to the previous models. In addition, we observe that the presence of the jet component increases the overall polarization signal and the energy of the jet component also has an impact. Model *Jet51* shows the highest level of polarization out of the three models in

rizJ filters. This could be due to a further break in symmetry in these models due to the presence of the jet. In Fig. 1, we can see scattering opacity present in the jet direction, which is more prominent in the Jet51 case. This can scatter and polarize the photons that add to the detected polarization signal. We see the highest levels of polarization from intermediate angles of 26° and 66° .

For model Wind, we overall do not see a significant polarization signal for any epoch. In the case of model Jet49, we detect negative Stokes q for shorter wavelengths at 1.3 and 2.4 d after the merger. However, for 3.8 and 4.2 d after the merger, the polarization signal is positive Stokes q at wavelengths between 1.0 and $1.75\ \mu\text{m}$. For model Jet51, the sign of Stokes q depends on the viewing angles. For 26° , we observe positive Stokes q for all the epochs and wavelengths; however, for other angles the sign of q flips from some negative to overall positive at days after 3.8. Hence, observation of significant polarization from KN can help us differentiate between the structure with or without the jet, and also the sign of observed Stokes q can help with constraining the energetics of the jet.

As mentioned in Section 2, all three models assume a lanthanide-poor composition for the ‘secular’ ejecta since a lanthanide-rich composition is expected to give no polarization. Polarimetric observations of future KNe will help constrain the composition of the ejecta and provide a smoking gun for the presence (detection) or absence (non-detection) of a lanthanide-poor component (Bulla et al. 2019, 2021).

Polarization curves along with light curves can constrain the inclination angle of the system. If the density distribution is constrained via light curves, then we can use polarization measurements to constrain the inclination angle. Depending on the model, the detectable polarization signal depends on the viewing angle and time since the merger. Thus, our models show that the combined observations of polarimetry and photometry will be powerful in our understanding of the KN ejecta structure.

4.1 AT2017gfo

One of the most well-studied KNe so far is the one associated with the GW event GW170817, namely AT2017gfo (Coulter et al. 2017). There are extensive observational data on this event, from spectra and light curves to polarization observations. In Fig. 2, we have overplotted AT2017gfo observations data as the open circles for all the filters. We find that our models predict higher apparent magnitudes compared to the previous model by Nativi et al. (2021). This higher apparent magnitude is closer to the observational data from AT2017gfo (Andreoni et al. 2017; Arcavi et al. 2017; Chornock et al. 2017; Cowperthwaite et al. 2017; Drout et al. 2017; Evans et al. 2017; Kasliwal et al. 2017; Pian et al. 2017; Smartt et al. 2017; Tanvir et al. 2017; Troja et al. 2017; Utsumi et al. 2017; Valenti et al. 2017). Qualitatively, we find a similar general trend between the observations and the models. However, we do not find one particular inclination angle to match the observational data. From the observed superluminal motion of the jet in radio images, Mooley, Anderson & Lu (2022) constrained the inclination angle to $\sim 19\text{--}25^\circ$ for AT2017gfo. We find that the models with Jet match better with the observed values at an inclination angle closer to 25° ($\cos \theta_{\text{obs}} = 0.9$). However, we note that these simulations were not performed for AT2017gfo but were more generalized scenarios.

Covino et al. (2017) reported a low level of linear optical polarization signal for AT2017gfo. With 5σ significance, they observed a polarization value of 0.5 ± 0.7 per cent at 1.46 d after the merger. They attribute this signal to interstellar polarization induced by Galactic dust and the KN being intrinsically unpolarized. This agrees

well with our polarization predictions from the models as shown via the polarization curve in Fig. 5. At 1.46 d after the merger, our models predict polarization less than 0.2 per cent for viewing angles $\lesssim 25^\circ$. In addition, recently Snepken et al. (2023) showed that AT2017gfo was a highly symmetric explosion at early times using the Sr + P Cygni profile along with KN blackbody features. Spherical ejecta would be consistent with the small polarization level observed in AT2017gfo, but potentially in conflict with numerical-relativity simulations (see Nakar 2020, for a review) and KN modelling suggesting the presence of at least two ejecta components with different geometries and compositions (e.g. Perego, Radice & Bernuzzi 2017; Kawaguchi et al. 2018; Bulla 2023).

5 CONCLUSIONS

We have presented results for the state-of-the-art 3D MCRT simulations using POSSIS. These simulations are an improvement over the previous models due to the realistic merger ejecta distribution and opacities for this ejecta and the evolution of these quantities with time. We present predictions of both photometric and polarimetric behaviour of the emission from binary NS mergers for the cases Wind, Jet49, and Jet51. From our simulations, we concluded the following:

- (i) Light curves from these simulations show that colour evolution is highly dependent on the presence of a jet. Thus, observations in a few different filters like u , g , and z can differentiate among these models.
- (ii) Polarimetric results show that the presence of a jet has some impact on the detected level of polarization. We see jets with higher energy produce a higher level of polarization.
- (iii) Observing polarization evolution with time in a few filters such as *rizJ* filters can help us differentiate among different density structures.

We note, however, that the predicted level of polarization is generally low. This is likely model-dependent given our choice to focus on specific realizations of binary NS mergers. In contrast, the increase in polarization from the presence of a jet is likely more robust due to the expectation that the jet will spread out electron-scattering plumes to wider regions.

The analysis presented in this work demonstrates how the combination of light curves and polarimetric observations of KN in a few different filters can provide valuable information about the event such as its inclination angle and the presence of a jet in the ejecta. The predicted low levels of polarization make observations with current polarimeters a challenge for a new KN in the near future. However, with future, more sensitive polarimeters, this level of polarization can be observable. Currently, observers can utilize these simulations to prepare for the best observing strategies for future KNe.

ACKNOWLEDGEMENTS

The simulations were performed on resources provided by the Swedish National Infrastructure for Computing (SNIC) at Kebnekaise partially funded by the Swedish Research Council through grant agreement no. 2018-05973, as well as on the GCS Supercomputer SuperMUC-NG at the Leibniz Supercomputing Centre (LRZ) (project pn29ba). MS was supported by an Science and Technology Facilities Council (STFC) consolidated grant no. ST/R000484/1 to LJMU. This work was supported by the European Union’s Horizon 2020 Programme under the AHEAD2020 project (grant agreement no. 871158). SR has been supported by the Swedish

Research Council (VR) under grant no. 2020-05044, by the research environment grant ‘Gravitational Radiation and Electromagnetic Astrophysical Transients’ (GREAT) funded by the Swedish Research Council (VR) under grant no. 2016-06012, by the Knut and Alice Wallenberg Foundation under grant no. KAW 2019.0112, by the Deutsche Forschungsgemeinschaft (DFG, German Research Foundation) under Germany’s Excellence Strategy – EXC 2121 ‘Quantum Universe’ – 390833306, and by the European Research Council (ERC) Advanced Grant INSPIRATION under the European Union’s Horizon 2020 research and innovation programme (grant agreement no. 101053985).

DATA AVAILABILITY

The light curves for the models used in this study will be made available at https://github.com/mbulla/kilonova_models. The POSSIS code used to simulate the light curves is not publicly available.

REFERENCES

- Abbott D. C., Lucy L. B., 1985, *ApJ*, 288, 679
 Abbott B. P. et al., 2017, *Phys. Rev. Lett.*, 119, 161101
 Alexander K. D. et al., 2017, *ApJ*, 848, L21
 Andreoni I. et al., 2017, *Publ. Astron. Soc. Aust.*, 34, e069
 Arcavi I. et al., 2017, *Nature*, 551, 64
 Barnes J., Kasen D., Wu M.-R., Martínez-Pinedo G., 2016, *ApJ*, 829, 110
 Beloborodov A. M., 2008, in Axelsson M. ed., AIP Conf. Proc. Vol. 1054, Cool Disks, Hot Flows: The Varying Faces of Accreting Compact Objects. Am. Inst. Phys., New York, p. 51
 Bulla M., 2019, *MNRAS*, 489, 5037
 Bulla M., 2023, *MNRAS*, 520, 2558
 Bulla M., Sim S. A., Kromer M., 2015, *MNRAS*, 450, 967
 Bulla M. et al., 2019, *Nat. Astron.*, 3, 99
 Bulla M. et al., 2021, *MNRAS*, 501, 1891
 Charalampopoulos P., Bulla M., Bonnerot C., Leloudas G., 2022, *A&A*, 670, A150
 Chornock R. et al., 2017, *ApJ*, 848, L19
 Collins C. E., Bauswein A., Sim S. A., Vijayan V., Martínez-Pinedo G., Just O., Shingles L. J., Kromer M., 2022, *MNRAS*, 521, 1858
 Coulter D. A. et al., 2017, *Science*, 358, 1556
 Covino S. et al., 2017, *Nat. Astron.*, 1, 791
 Cowperthwaite P. S. et al., 2017, *ApJ*, 848, L17
 Darbha S., Kasen D., 2020, *ApJ*, 897, 150
 Domoto N., Tanaka M., Wanajo S., Kawaguchi K., 2021, *ApJ*, 913, 26
 Drout M. R. et al., 2017, *Science*, 358, 1570
 Eichler D., Livio M., Piran T., Schramm D. N., 1989, *Nature*, 340, 126
 Evans P. A. et al., 2017, *Science*, 358, 1565
 Fernández R., Tchekhovskoy A., Quataert E., Foucart F., Kasen D., 2019, *MNRAS*, 482, 3373
 Freiburghaus C., Rosswog S., Thielemann F.-K., 1999, *ApJ*, 525, L121
 Goldstein A. et al., 2017, *ApJ*, 848, L14
 Haggard D., Nynka M., Ruan J. J., Kalogera V., Cenko S. B., Evans P., Kennea J. A., 2017, *ApJ*, 848, L25
 Inarra C., Bulla M., Sim S. A., Smartt S. J., 2016, *ApJ*, 831, 79
 Just O., Bauswein A., Ardevol Pulpillo R., Goriely S., Janka H. T., 2015, *MNRAS*, 448, 541
 Kasliwal M. M. et al., 2017, *Science*, 358, 1559
 Kasliwal M. M. et al., 2022, *MNRAS*, 510, L7
 Kawaguchi K., Shibata M., Tanaka M., 2018, *ApJ*, 865, L21
 Klion H., Duffell P. C., Kasen D., Quataert E., 2021, *MNRAS*, 502, 865
 Korobkin O. et al., 2021, *ApJ*, 910, 116
 Lattimer J. M., Schramm D. N., 1974, *ApJ*, 192, L145
 Leloudas G. et al., 2022, *Nat. Astron.*, 6, 1193
 Li L.-X., Paczyński B., 1998, *ApJ*, 507, L59
 Li Y., Shen R.-F., 2019, *ApJ*, 879, 31
 Lucy L. B., 1999, *A&A*, 344, 282
 Margutti R. et al., 2017, *ApJ*, 848, L20
 Matsumoto T., 2018, *MNRAS*, 481, 1008
 Miller J. M. et al., 2019, *Phys. Rev. D*, 100, 023008
 Mooley K. P., Anderson J., Lu W., 2022, *Nature*, 610, 273
 Nakar E., 2020, *Phys. Rep.*, 886, 1
 Nativi L., Bulla M., Rosswog S., Lundman C., Kowal G., Gizzi D., Lamb G. P., Perego A., 2021, *MNRAS*, 500, 1772
 Perego A., Rosswog S., Cabezón R. M., Korobkin O., Käppeli R., Arcones A., Liebendörfer M., 2014, *MNRAS*, 443, 3134
 Perego A., Radice D., Bernuzzi S., 2017, *ApJ*, 850, L37
 Pian E. et al., 2017, *Nature*, 551, 67
 Rastinejad J. C. et al., 2022, *Nature*, 612, 223
 Rosswog S., Korobkin O., 2022, preprint (arXiv:2208.14026)
 Rosswog S., Liebendörfer M., Thielemann F.-K., Davies M., Benz W., Piran T., 1999, *A&A*, 341, 499
 Savchenko V. et al., 2017, *ApJ*, 848, L15
 Schafly E. F., Finkbeiner D. P., 2011, *ApJ*, 737, 103
 Siegel D. M., Metzger B. D., 2018, *ApJ*, 858, 52
 Smartt S. J. et al., 2017, *Nature*, 551, 75
 Sneppe A., Watson D., Bauswein A., Just O., Kotak R., Nakar E., Poznanski D., Sim S., 2023, *Nature*, 614, 436
 Soares-Santos M. et al., 2017, *ApJ*, 848, L16
 Symbolist E., Schramm D. N., 1982, *Astrophys. Lett.*, 22, 143
 Tanaka M., Kato D., Gaigalas G., Kawaguchi K., 2020, *MNRAS*, 496, 1369
 Tanvir N. R., Levan A. J., Fruchter A. S., Hjorth J., Hounsell R. A., Wiersema K., Tunnicliffe R. L., 2013, *Nature*, 500, 547
 Tanvir N. R. et al., 2017, *ApJ*, 848, L27
 Troja E. et al., 2017, *Nature*, 551, 71
 Troja E. et al., 2022, *Nature*, 612, 228
 Utsumi Y. et al., 2017, *PASJ*, 69, 101
 Valenti S. et al., 2017, *ApJ*, 848, L24
 Watson D. et al., 2019, *Nature*, 574, 497
 Wollaeger R. T. et al., 2018, *MNRAS*, 478, 3298

This paper has been typeset from a \LaTeX file prepared by the author.